Hindawi
Geofluids
Volume 2017, Article ID 1206587, 18 pages
https://doi.org/10.1155/2017/1206587

Research Article

Genesis of the Bairendaba Ag-Zn-Pb Deposit, Southern Great Xing'an Range, NE China: A Fluid Inclusion and Stable Isotope Study

Shunda Li, Keyong Wang, Yicun Wang, Xuebing Zhang, and Hongyan Quan

College of Earth Sciences, Jilin University, Changchun 130061, China

Correspondence should be addressed to Keyong Wang; wangky@jlu.edu.cn

Received 24 March 2017; Revised 24 May 2017; Accepted 12 June 2017; Published 13 July 2017

Academic Editor: Bin Chen

The Bairendaba deposit is the largest Ag-Zn-Pb deposit in Inner Mongolia. Vein and disseminated ores occur in biotite-plagioclase gneiss and quartz diorite along regional EW trending faults. Microthermometric data for H_2O-NaCl ± CH_4 ± CO_2 fluid inclusions record a decrease in homogenization temperature and salinity of ore-forming fluids with time. Early and main-stage mineralization have homogenization temperatures of 242°–395°C and 173°–334°C, respectively, compared with 138°–213°C for late-stage mineralization. Fluid salinities for early mineralization have a bimodal distribution, dominantly 4.2–11.8 wt.% NaCl equivalent, with 35.2–37.8 wt.% NaCl equivalent for a small population of halite-bearing inclusions. Main- and late-stage fluids have salinities of 2.1–10.2 wt.% NaCl equivalent and 0.7–8.4 wt.% NaCl equivalent, respectively. Oxygen and hydrogen isotope data indicate the interaction of a magmatic fluid with wall rocks in early mineralization, followed by the introduction of meteoric water during late-stage mineralization. Values of –15.9‰ to –12‰ ($\delta^{13}C_{PDB}$) for hydrothermal quartz indicate that organic-rich strata were the source of carbon. Sulfur had a magmatic source, based on values of –0.1‰ to 1.5‰ ($\delta^{34}S_{V\text{-}CDT}$) for sulfide minerals. The Bairendaba deposit is a typical mesothermal system with mineralization controlled by structure.

1. Introduction

The southern Great Xing'an Range (SGXR) occurs in southeastern Inner Mongolia and is an important metallogenic belt in China [1–3]. It is bounded by the Hegenshan-Heihe and Xar Moron faults to the north and south, respectively, and Songliao Basin to the east (Figure 1(a)). More than fifty deposits have been discovered in this area since the 1970s, including those of Bairendaba, Mengentaolegai, Aerhada, Huaaobaote, Daolundaba, and Shuangjianshan [4–9]. These deposits occur along northeast (NE) and EW trending faults, with host rocks being mainly Permian strata. Mineralization is related to magmatic-hydrothermal activity associated with Jurassic and Cretaceous intrusions [2, 10, 11].

The large Ag-Zn-Pb Bairendaba deposit occurs on the western edge of the SGXR (Figure 1(a)). It was discovered in 2001 by the Ninth Geological Prospecting Institute of Inner Mongolia and initially developed by local prospectors. The deposit is now worked by the Inner Mongolia Yindu Mining Co. Ltd. and has proven reserves of 1.4 million t Zn, 0.6 million t Pb, and 4.6 thousand t Ag. Recent studies have examined geological features, alteration, sulfur isotopes, dating of mineralization, and the origin of ore-forming fluids [12–20]. However, additional data are necessary to better characterize the mineralizing fluids and understand ore deposition in the different stages of mineralization.

Data compiled from detailed field investigations were used to select samples of quartz and fluorite, from ore veins, for this study. Fluid inclusion petrography, microthermometry, and laser Raman microprobe analyses generated data to determine phase ratios, volatile constituents, and trapping temperatures for the ore-forming fluids. Types of fluids inclusions in different veins were also determined to document changes and evolution of the hydrothermal system. Origins of fluids that formed the orebodies are based on new oxygen (O), hydrogen (H), carbon (C), and sulfur

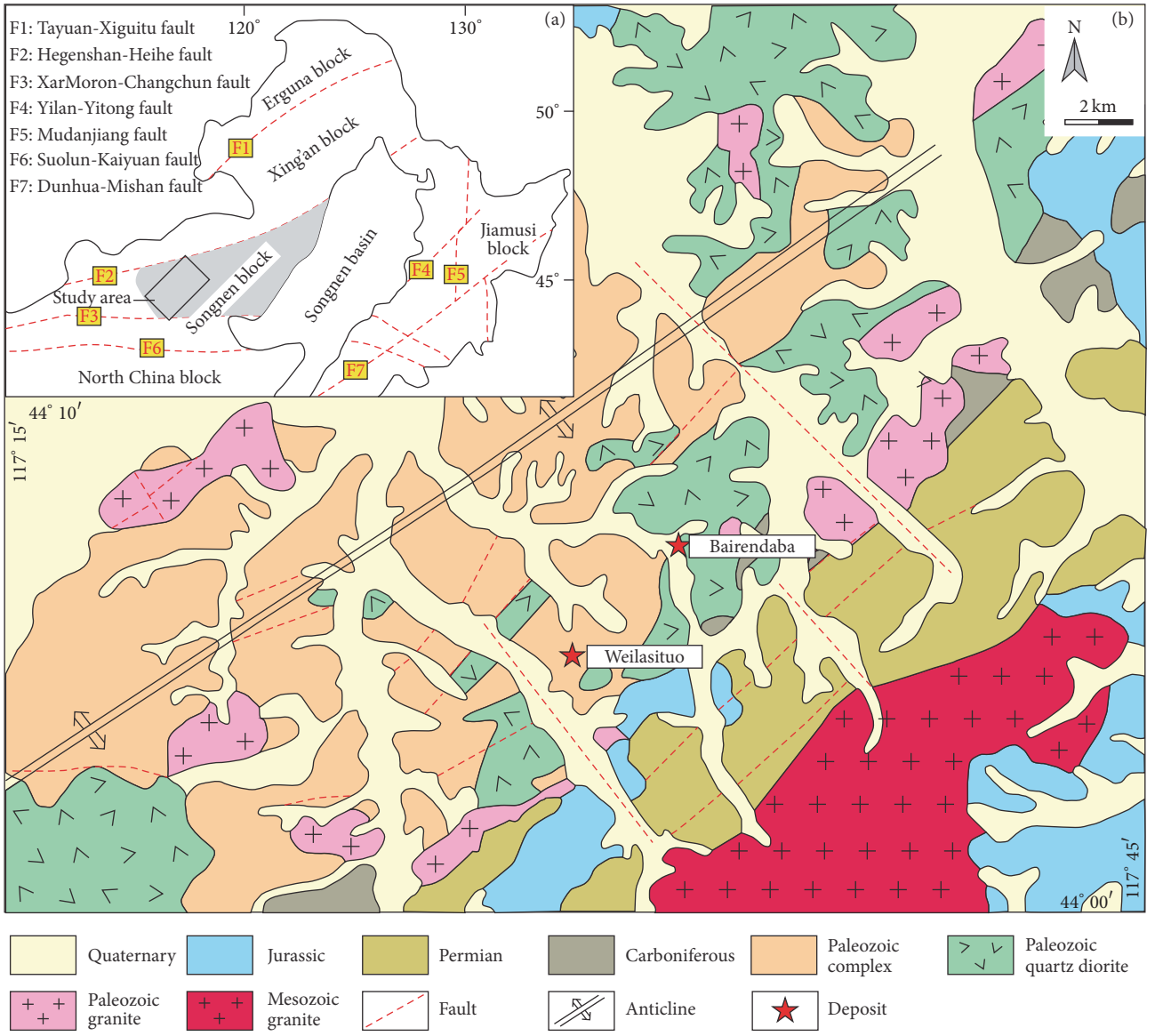

FIGURE 1: (a) Tectonic map of northeastern China [29]. (b) Regional geological map of the Bairendaba district [30].

(S) isotope data. By combining the results of fluid inclusion and stable isotope studies, a genetic model is proposed for the Bairendaba Ag-Zn-Pb deposit.

2. Geologic Background

2.1. Regional Geology. Rock units in the Bairendaba district include an assemblage of Carboniferous, Permian, Jurassic, and Quaternary units surrounding a medium- to high-grade metamorphic complex of amphibole-plagioclase gneiss and biotite-plagioclase gneiss (Figure 1(b)) that yield U-Pb ages of 437 ± 3 to ~316 ± 3 Ma [21, 22]. Carboniferous strata consist of marine carbonates, in contrast to Permian strata of silty slate, clastic, and volcanic rocks. Fossiliferous Permian rocks rich in organic carbon represent the main host for Ag-Zn-Pb ± Cu mineralization [23–27]. Lacustrine sedimentary and continental silicic volcanic rocks make up the Jurassic strata [28]. All rock units are partially covered by unconsolidated Quaternary sediments.

Significant bodies of Paleozoic and Mesozoic intrusive igneous rocks occur throughout the region (Figure 1(b)). Paleozoic granitoids include diorite and tonalite that yield U-Pb ages of 323.9–326.5 Ma [14, 15]. These rocks constitute a high-potassium, calc-alkaline magmatic suite produced under a geodynamic regime of the Paleo-Asian Ocean slab break-off [31]. Surface exposure of Mesozoic granitoids is limited to the Beidashan granitic batholith, ~5 km southeast of the Bairendaba deposit (Figure 1(b)). The mineral composition of the granitoids is mainly quartz, plagioclase feldspar, potassium feldspar, and biotite. These granitoids yield ages

of 139-140 Ma [30] and are characterized by high-silica and high-alkaline types [22], indicating formation within the Circum-Pacific tectonic domain.

The Bairendaba deposit occurs in Carboniferous and Permian strata comprising the southeast limb of a NE trending anticline, with a core of Paleoproterozoic metamorphic rocks (Figure 1(b)). Three groups of regional faults are distinguished by their trend and style of deformation. Faults with NE trends exhibit compressional shearing, EW faults are extensional-shearing, and faults with northwest (NW) trends produced extension.

2.2. Deposit Geology and Mineralization. Three regional-fault trends are present at the mine scale and cut units of Paleozoic biotite-plagioclase gneiss and amphibole-plagioclase gneiss that strike N36 to ~61E and dip at 35° to ~58° to the northwest (Figure 2(a)). Northeast-trending faults formed in the Hercynian, whereas EW and NW trending faults formed in the Yanshanian. Orebodies at the Bairendaba deposit occur dominantly in EW faults, with NW trending faults being a secondary control on mineralization.

Intermediate-silicic igneous rocks are common in the region and occur as stocks and dykes at the Bairendaba deposit (Figure 2(a)). Devonian granite, with a SHRIMP U-Pb age of 382 ± 2 Ma [32], represents the first phase of igneous activity and occurs in the northeastern part of the deposit. A SHRIMP U-Pb age of 326.5 ± 1.6 Ma dates the high-potassium calc-alkaline Carboniferous quartz diorite [15], which is cut by dolerite and granite dykes with U-Pb ages of 314.1 ± 1.7 Ma and 318 ± 1.2 Ma, respectively [33].

Exploration of the Bairendaba deposit has discovered 54 orebodies, including 34 concealed orebodies. The bedded-type orebodies occur in biotite-plagioclase gneiss and adjacent quartz diorite. Most orebodies strike EW and dip at 8° to ~50° to the NW, with a smaller group that strike NW and dip at 26° to ~34° to the NE (Figure 2(a)).

The number 1 orebody hosts 84% of proven reserves, and ore grades are 251.5 g/t Ag, 2.8 wt.% Pb, and 6.0 wt.% Zn [34]. This economically significant orebody occurs within altered quartz diorite and is 2075 m long, has an average thickness of 3.6 m, and extends to a depth of ~1135 m (Figure 2(b)). It strikes EW and dips at 16° to ~51°, mainly to the north.

Ores textures are varied and include euhedral-subhedral crystals, metasomatic dissolution features, banding, veins, disseminations, and fillings of miarolitic cavities (Figures 3(e)–3(h)). The assemblage of sulfide minerals includes arsenopyrite, pyrite, pyrrhotite, sphalerite, chalcopyrite, and galena, along with minor tetrahedrite, pyrargyrite, and argentite (Figures 3(e)–3(h)). Gangue minerals are quartz, fluorite, calcite, sericite, and epidote.

Wall-rock alteration is intense and consists of silicification, sericitization, chloritization, carbonatization, and kaolin, followed by epidotization with pyrophyllite. Silicification, chloritization, and sericitization are closely associated with Ag-Pb-Zn mineralization [18, 35].

The Bairendaba deposit contains numerous hydrothermal veins of different scale (Figures 3(a)–3(d)). Hypogene fissure-filling mineralization is divided into three paragenetic stages (Figure 4), based on ore mineralogy and cross-cutting relationships. These stages are recognized by four types of hydrothermal veins.

Early mineralization (Stage 1) is subeconomic and consists of quartz-pyrite-arsenopyrite veins (A veins; Figure 3(a)). The main stage of mineralization (Stage 2) is widespread and yields the majority of Ag-Zn-Pb production. Characteristic minerals are milky white quartz, chalcopyrite, pyrrhotite, sphalerite, and galena, along with minor pyrargyrite, sericite, and chlorite. Stage 2 mineralization is divided into quartz-pyrrhotite-chalcopyrite-sphalerite veins (B veins, Stage 2-1; Figure 3(b)) and Ag-sulfide quartz veins (C veins, Stage 2-2; Figure 3(c)), respectively. Late-stage mineralization (Stage 3) consists of sulfide-poor calcite and fluorite veins (D veins), which have a limited distribution near the outer edge of the deposit (Figure 3(d)).

2.3. Timing of Mineralization. Age data for the Bairendaba deposit indicate mineralization and alteration occurred in the Early Cretaceous. Rb-Sr dating of sphalerite, in a quartz vein, yielded an isochron age of 116 Ma [17] that is appreciably younger than the 139 to ~140 Ma Mesozoic granitoids and does not support ore formation through magmatic-hydrothermal processes. However, an $^{40}Ar/^{39}Ar$ age of 133 ± 2 Ma for sericite [14] is consistent with mineralization being associated with Mesozoic igneous rocks.

3. Samples and Analytical Methods

Fluid inclusions were studied in samples of quartz and fluorite of vein types A–D, representing Stages 1–3. Fluid inclusion microthermometric analyses were conducted on a Linkam THMS600 heating-freezing stage with a temperature range of –196 to 600°C. Calibration of the stage was completed using the following standards: pure water inclusions (0°C), pure CO_2 inclusions (–56.6°C), and potassium bichromate (398°C). This yielded an accuracy of ±0.2°C during freezing and ±2°C for heating between 100° and 600°C. Fluid salinities for NaCl-H_2O inclusions were calculated using the final melting temperature of ice [36].

Fluid inclusion volatiles were analyzed using a Renishaw RM1000 Raman microprobe and Ar ion laser. Operating conditions for the Raman microprobe include the following: a surface power of 5 mW and exciting radiation of 514.5 nm; area of 20 μm^2 for the detector charge-coupled device (CCD); spectra set to scanning range of 1000 to 4000/cm with an accumulation time of 30 s per scan. All fluid inclusion studies were conducted at the Geological Fluid Laboratory, College of Earth Science, Jilin University, China.

Samples of hydrothermal quartz from Stages 1-2, excluding D veins, were analyzed for O-H-C isotopes. Quartz samples for O-C isotope analyses were treated with orthophosphoric acid at 50°C for 24 h to generate CO_2 [37]. Samples of quartz for H isotope analyses were placed under vacuum and heated at 150°C for 3 h to degas labile volatiles. Water was released from fluid inclusions by heating to approximately 500°C, using an induction furnace, and then converted into H_2 through interaction with Zn powder at a temperature of 410°C [38]. Finally, conventional methods were used to produce SO_2 gas from different sulfide minerals to measure

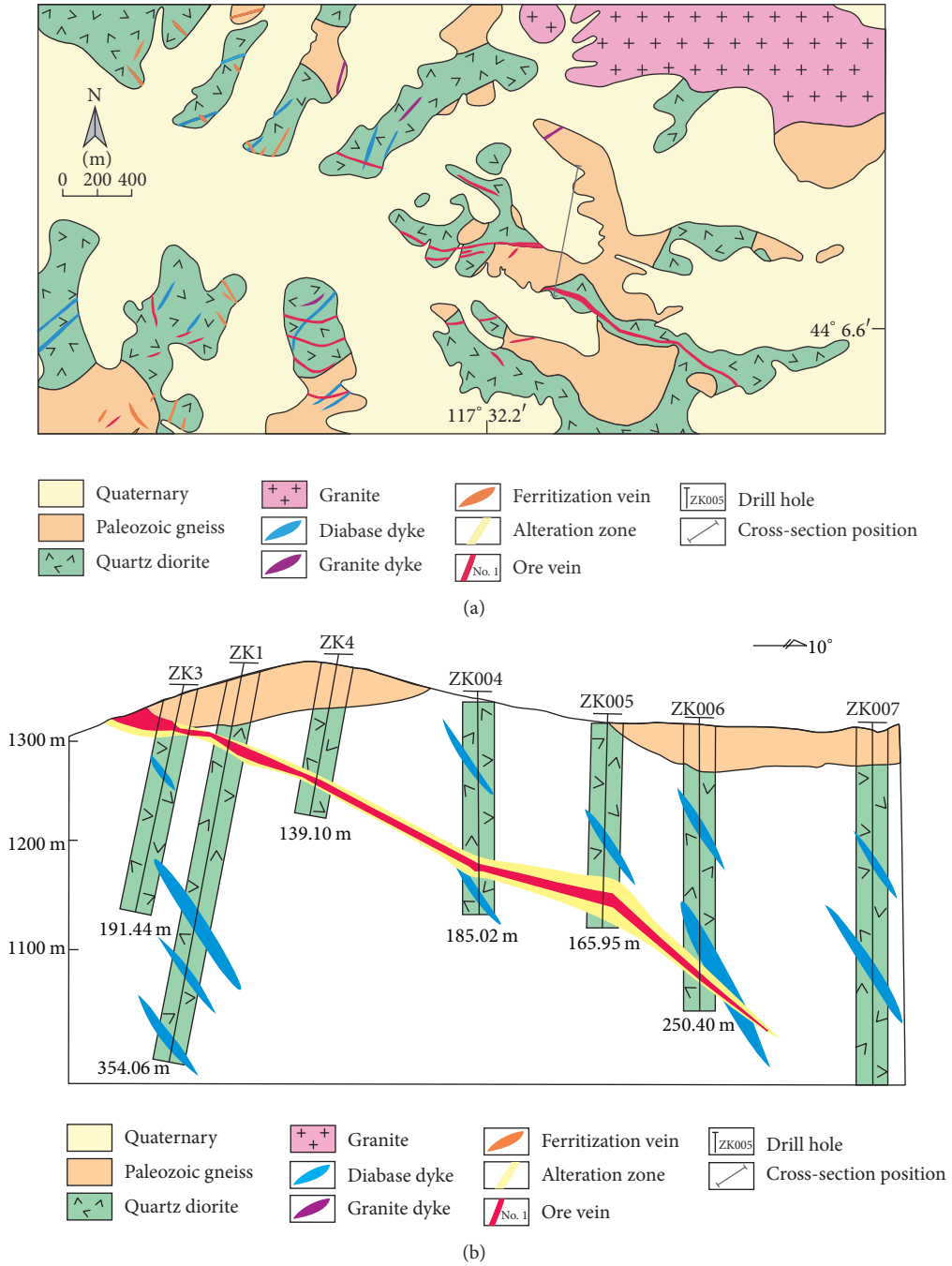

Figure 2: (a) Geological map of the Bairendaba Ag-Zn-Pb deposit (after the Ninth Geological Prospecting Institute of Inner Mongolia 2004). (b) Geological cross-section of the number 1 ore body (after the Ninth Geological Prospecting Institute of Inner Mongolia 2004).

S isotopes [39]. All samples were analyzed using a MAT-252 mass spectrometer, with analytical uncertainty of <0.1‰, housed at the Analytical Laboratory Beijing Research Institute of Uranium Geology, China.

4. Results

4.1. Fluid Inclusion Petrography. Criteria established by Roedder [40] and Hollister and Burruss [41] were used to distinguish different generations of fluid inclusions in hydrothermal quartz and fluorite. Primary inclusions are isolated or occur in random groups, compared with secondary inclusions filling microcracks. Populations of different fluid inclusion types were recognized by room temperature phase relationships, phase transitions during heating and cooling, and laser Raman spectroscopy results. Four types of fluid inclusions were identified using the nomenclature of Ramboz et al. [42], which are CH_4-rich (Type I), CH_4-CO_2-H_2O

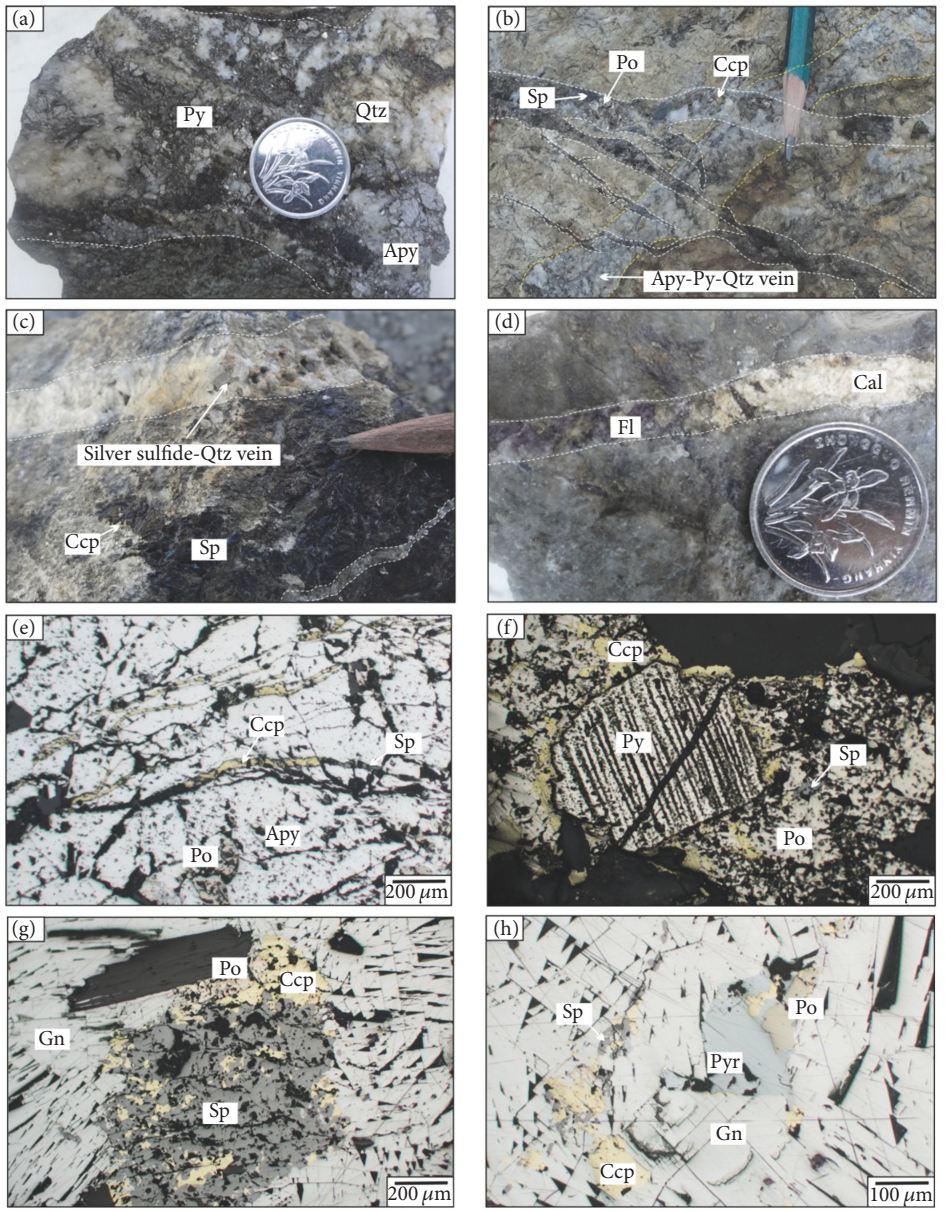

Figure 3: Photographs and photomicrographs of ore from the Bairendaba Ag-Zn-Pb deposit. (a) Quartz-pyrite-arsenopyrite vein. (b) Quartz-pyrite-arsenopyrite vein cut by quartz-pyrrhotite-chalcopyrite-sphalerite vein. (c) Quartz-pyrrhotite-chalcopyrite-sphalerite vein cut by Ag-sulfide quartz vein. (d) Calcite-fluorite vein. (e) Galena cut by chalcopyrite-sphalerite vein. (f) Pyrite replaced by pyrrhotite-chalcopyrite-sphalerite aggregate. (g) Pyrrhotite-chalcopyrite-sphalerite aggregate replaced by galena. (h) Pyrargyrite in galena. Qz (quartz); Po (pyrrhotite); Py (pyrite); Ccp (chalcopyrite); Sp (sphalerite); Gn (galena); Pyr (pyrargyrite).

(Type II), H_2O-rich (Type III), and halite-bearing (Type IV) types.

Type I inclusions consist of liquid water and CH_4 at room temperature, with a degree of fill ranging from 0.2 to ~0.6 (Figure 5(a)). These inclusions are common in A veins (Stage 1) and occur as bands or clusters or in isolation. They have irregular or negative crystal shapes and are typically 10 to 30 μm in size.

Type II inclusions appear similar to Type I at room temperature (Figures 5(d)–5(f)). However, the addition of a CO_2 component to CH_4 in Type II inclusions is evident during freezing and laser Raman microprobe measurements. These inclusions are absent from A veins and can occur in isolation but are more common as clusters and trails in B and C veins (Stage 2). They have regular shapes (e.g., ellipsoidal or negative crystal) and are 10 to 30 μm in size.

Type III fluid inclusions are liquid water dominant and have vapor contents of 10% to ~45% and variable shapes (e.g., irregular and ellipsoidal), ranging in size from 5 to 20 μm (Figures 5(c), 5(g)–5(i)). These inclusions are present in all stages of mineralization and commonly occur as planar arrays restricted to the interiors of quartz and fluorite grains.

Period/stages / Minerals	Hydrothermal period				Supergene period
	Stage 1	Stage 2-1	Stage 2-2	Stage 3	
Arsenopyrite					
Pyrite					
Pyrrhotite					
Chalcopyrite					
Sphalerite					
Galena					
Pyrargyrite					
Argentite					
Limonite					
Malachite					
Quartz					
Sericite					
Calcite					
Epidote					
Fluorite					
Veins	A veins	B veins	C veins	D veins	
System	$NaCl\text{-}H_2O\text{-}CH_4\text{-}CO_2$			$NaCl\text{-}H_2O$	

Figure 4: Mineral paragenesis for the Bairendaba Ag-Zn-Pb deposit.

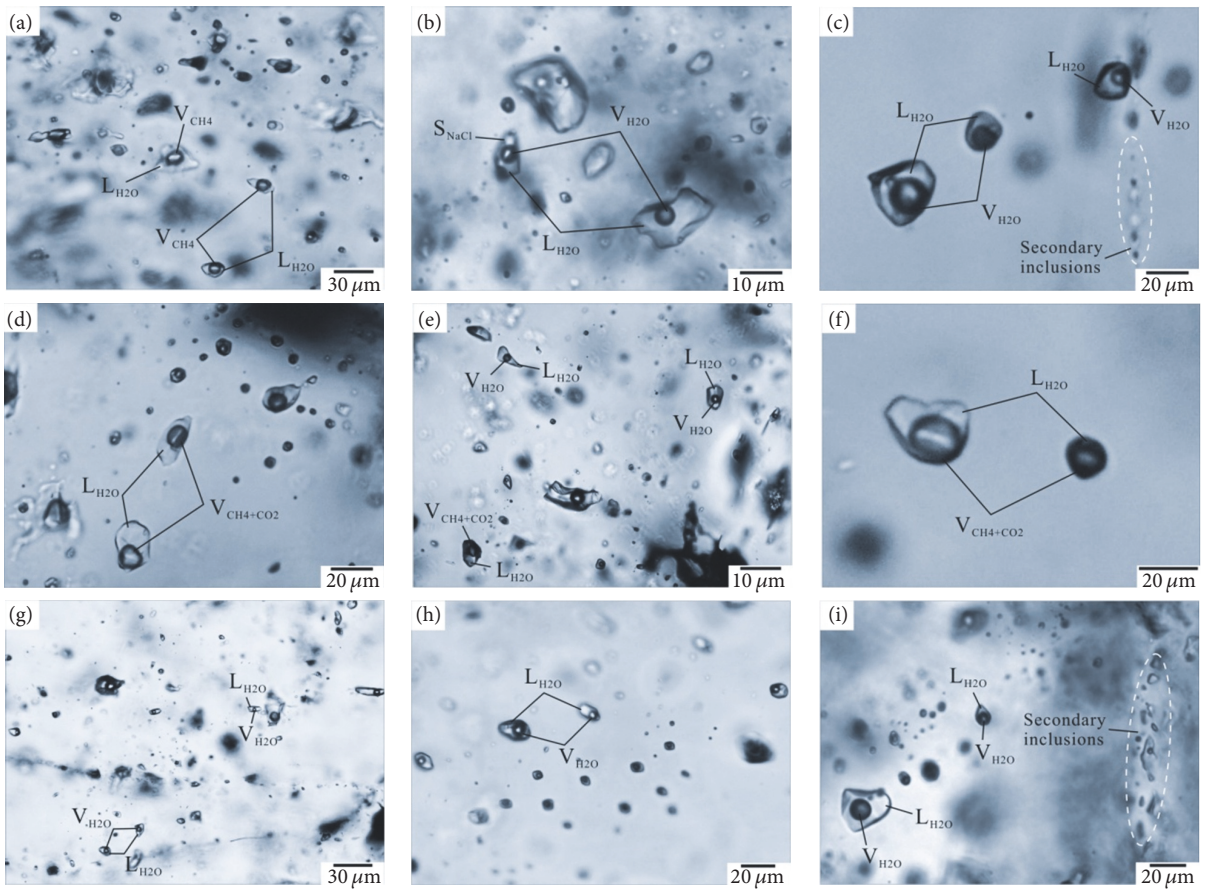

Figure 5: Photomicrographs of fluid inclusions in Stages 1–3 quartz and fluorite in the Bairendaba Ag-Zn-Pb deposit. ((a), (b), (c)) Type I, Type III, and Type IV inclusions in Stage 1 quartz. ((d), (e)) Type II and Type III inclusions in Stage 2-1 quartz. ((f), (g)) Type II and Type III inclusions in Stage 2-1 quartz. ((h), (i)) Type III inclusions in Stage 3 fluorite. L (liquid phase), V (vapor phase), and S (halite crystal).

However, some Type III inclusions fill microfractures in Stages 1-2 quartz and Stage 3 fluorite, indicating a secondary origin (Figures 5(c) and 5(i)).

Type IV fluid inclusions contain three phases at room temperature, which are a vapor bubble, liquid water, and halite cube (Figure 5(b)). Halite-bearing inclusions are uncommon and coexist with Types I and III in A veins of Stage 1 mineralization. Type IV inclusions are always <20 μm in size and occur in isolation or discrete clusters, implying a primary origin [40].

4.2. Fluid Inclusion Microthermometry. Primary fluid inclusions larger than 5 μm with a regular crystal shape, which show no signs of necking [40], were chosen for microthermometric analyses. Data for Stages 1–3 are listed in Table 1. Histograms of homogenization temperatures (Th) and salinity of different types of fluid inclusions in Stages 1-2 quartz and Stage 3 fluorite are presented in Figure 6.

Stage 1 quartz veins contain abundant Type I and III fluid inclusions, but rare Type IV inclusions. Type I inclusions freeze below –185°C and melting of the carbonic phase (Tm_{CO2}) occurs at –182.1° to –180.2°C (Table 1). This behavior indicates the vapor phase is nearly pure CH_4. Homogenization of the carbonic phase (Th_{CO2}) to vapor occurs at –99.3° to –68.4°C, and clathrate melting (Tm_{Clath}) between 11.2° and 18.9°C (Table 1) is much higher than the invariant point (e.g., 10°C) of a pure CO_2 clathrate [41]. Type I inclusions with a high degree of fill decrepitate at ~350°C, prior to final homogenization, probably due to increased internal pressures of CH_4 [40]. In contrast, Type I inclusions with a low degree of fill have Th of 267°–395°C (Figure 6(a)). Type III inclusions homogenize to the liquid phase at 242°–351°C (Figure 6(a)) and final ice melting at –8.1° to –2.5°C indicates salinities of 4.2–11.8 wt.% NaCl equivalent (Figure 6(b)). Halite crystals in Type IV inclusions dissolve at 258°–295°C, indicating salinities of 35.2–37.8 wt.% NaCl equivalent, and they have final homogenization to the liquid phase at 259°–372°C (Figures 6(a) and 6(b)).

Stage 2-1 and 2-2 quartz veins contain Type II and III fluid inclusions. Fluid inclusion data for Stage 2-1 are presented first. Type II inclusions freeze below –130°C and Tm_{CO2} occurs between –79.5° and –59.6°C (Table 1), significantly lower than melting of pure CO_2 at –56.6°C. This indicates the carbonic phase, which is mostly CH_4, also contains CO_2 and/or N_2 [42]. Homogenization of the carbonic phase to vapor occurs between –52.1° and 2.8°C and Tm_{Clath} at 7.9° to 16.8°C (Table 2). Final homogenization to the liquid phase could only be determined for fluid inclusions with a low degree of fill and Th which are 246°–334°C (Figure 6(c)). Type III inclusions homogenize to the liquid phase at 205–312°C and final ice melting at –6.8° to –1.6°C indicates salinities of 2.7–10.2 wt.% NaCl equivalent (Figures 6(c) and 6(d)).

Fluid inclusion Types II and III, representing Stage 2-2, have lower Th and are less saline than Stage 2-1 (Figures 6(c)–6(f)). Type II inclusions freeze below –100°C and Tm_{CO2} occurs at –63.4° to –57.7°C (Table 2). This behavior is consistent with the presence of small concentrations of CH_4 and/or N_2 in addition to CO_2 [44–46]. Homogenization of the carbonic phase to vapor occurs at –6.9° to 10.2°C and Tm_{Clath} between 9.5° and 13.8°C (Table 2). Final homogenization to the liquid phase could only be determined for inclusions with a low degree of fill and occurs at 173°–282°C (Figure 6(e)). Type III inclusions homogenize to the liquid phase at 179°–269°C and final ice melting at –5.9° to –1.2°C indicates salinities of 2.1–9.1 wt.% NaCl equivalent (Figures 6(e) and 6(f)).

Fluorite veins representing Stage 3 contain only Type III fluid inclusions that record the lowest Th and salinities for the Bairendaba deposit (Figures 6(a)–6(h)). Homogenization to the liquid phase occurs at 138°–213°C and final ice melting at –5.4° to –0.4°C indicates salinities of 0.7–8.4 wt.% NaCl equivalent (Figures 6(g) and 6(h)).

4.3. Laser Raman Microprobe Analysis. The data obtained by laser Raman microprobe analyses of fluid inclusions in Stages 1-2 quartz and Stage 3 fluorite are presented in Figure 7. Type I inclusions for Stage 1 contain a vapor phase dominated by CH_4 (Figures 7(a) and 7(b)), whereas Type II inclusions for Stage 2 contain different amounts of CH_4 and CO_2 (Figures 7(c)–7(e)). No pure CO_2 inclusions were identified in this study. The vapor phase of Type III inclusions consists solely of water (Figure 7(f)).

4.4. Oxygen, Hydrogen, and Carbon Isotopes. Isotope data for 12 quartz samples representing A-C veins in the Bairendaba deposit are reported as $\delta^{18}O_{V\text{-}SMOW}$, $\delta D_{V\text{-}SMOW}$, and $\delta^{13}C_{PDB}$ values. Ranges in the data are limited and are as follows: 13.2‰ to 14.2‰ ($\delta^{18}O_{V\text{-}SMOW}$); –124.6‰ to –113.4‰ ($\delta D_{V\text{-}SMOW}$); –15.9‰ to –12.0‰ ($\delta^{13}C_{PDB}$; Table 2). Values of 1.8‰ to 7.9‰ ($\delta^{18}O_{H2O\text{-}SMOW}$; Table 2) were calculated using the formula of Clayton et al. [59] and Th of fluid inclusions. These δD and δ^{18}O values are consistent with previously published data [17, 33, 47, 60]. The C isotope data in this study are unique, because this is the first time C isotopes were measured for the gas phase of fluid inclusions in hydrothermal quartz representing Stages 1-2 of the Bairendaba deposit. Previous work by Ouyang [33] generated data strictly for Stage 3 fluorite-calcite veins.

4.5. Sulfur Isotopes. Sulfur isotope analyses were completed for mineral separates of pyrite, pyrrhotite, galena, and sphalerite extracted from ore veins. All data are reported as $\delta^{34}S_{V\text{-}CDT}$ values. Sulfide minerals from the number 1 orebody of the Bairendaba Ag-Zn-Pb deposit have a limited range of –0.1‰ to 1.5‰ (Table 3), which are consistent with previously published data [17, 33, 47].

5. Discussion

5.1. Sources of Ore-Forming Materials. Sulfur isotopes are an important tool for determining the source(s) of ore-forming materials in deposits [57, 61–63]. The Bairendaba Ag-Zn-Pb deposit has δ^{34}S values of –4.0‰ to 1.7‰ with an average of –1.0‰ (Figure 8). These data show a normal distribution (Figure 8) and are similar to δ^{34}S values of –3‰ to 1‰ reported for magmatic-hydrothermal deposits [57, 63, 64].

Table 1: Microthermometric data for fluid inclusions in hydrothermal quartz and fluorite, Bairendaba Ag-Zn-Pb deposit.

Stage	Host mineral	Inclusion Type	Tm(CO_2) (°C)	Th(CO_2) (°C)	Tm(clath) (°C)	Tm(ice) (°C)	Tm(NaCl) (°C)	Salinity (NaCl wt.%)	Th (°C)
Stage 1	Quartz	I (65)	−182.1 to −180.2	−99.3 to −68.4	11.2–18.9	NA	NA	NA	267–395
		III (39)	NA	NA	NA	−8.1 to −2.5	NA	4.2–11.8	242–351
		IV (5)	NA	NA	NA	NA	258–295	35.2–37.8	259–372
Stage 2-1	Quartz	II (62)	−79.5 to −59.6	−52.1 to −2.8	7.9–16.8	NA	NA	NA	246–334
		III (38)	NA	NA	NA	−6.8 to −1.6	NA	2.7–10.2	205–312
Stage 2-2	Quartz	II (65)	−63.4 to −57.7	−6.9 to 10.2	9.5–13.8	NA	NA	NA	173–282
		III (44)	NA	NA	NA	−5.9 to −1.2	NA	2.1–9.1	179–269
Stage 3	Fluorite	III (57)	NA	NA	NA	−5.4 to −0.4	NA	0.7–8.4	138–213

Tm(ice), temperature of final ice melting; Tm(NaCl), melting temperature of halite crystals; (65) is the number of inclusions measured.

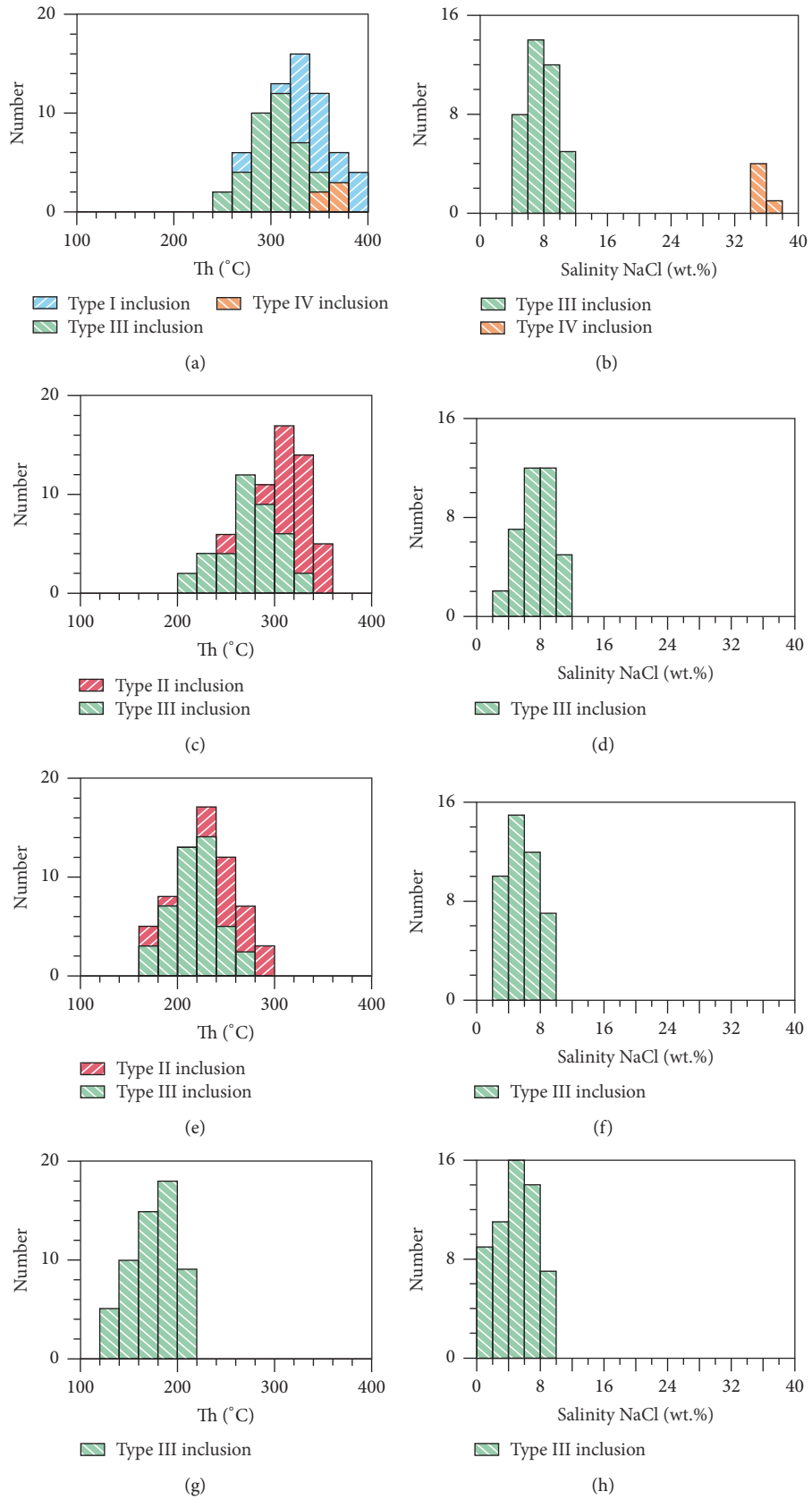

Figure 6: Histograms of microthermometric data for fluid inclusions in hydrothermal quartz and fluorite of the Bairendaba Ag-Zn-Pb deposit. (a) Homogenization temperatures for Types I, III, and IV; Stage 1 quartz. (b) Salinity for Types III and IV; Stage 1 quartz. (c) Homogenization temperatures for Types II and III; Stage 2-1 quartz. (d) Salinity for Type III; Stage 2-1 quartz. (e) Homogenization temperatures for Types II and III; Stage 2-2 quartz. (f) Salinity for Type III; Stage 2-2 quartz. (g) Homogenization temperatures for Type III; Stage 3 fluorite. (h) Salinity for Type III; Stage 3 fluorite.

Table 2: Oxygen, hydrogen, and carbon isotope data for hydrothermal quartz of Stages 1-2, Bairendaba Ag–Zn–Pb deposit.

Vein type	Stages	Sample description	$\delta^{18}O_{V\text{-}SMOW}$/%	$\delta D_{V\text{-}SMOW}$/%	Th (°C)	$\delta^{18}O_{H2O\text{-}SMOW}$/%	$\delta C_{V\text{-}PDB}$/%
A veins	1	Quartz	14.1	−113.4	320	7.9	−13.2
A veins	1	Quartz	14.2	−114.2	280	6.6	−12.8
A veins	1	Quartz	14.0	−114	320	7.8	−13.1
A veins	1	Quartz	14.1	−114.6	280	6.5	−12.9
B veins	2-1	Quartz	14.0	−116.2	300	7.1	−12.9
B veins	2-1	Quartz	13.9	−116.3	260	5.4	−15.8
B veins	2-1	Quartz	13.3	−116.7	300	6.4	−12.8
B veins	2-1	Quartz	13.2	−116.5	260	4.7	−15.7
C veins	2-2	Quartz	13.7	−117.4	240	4.3	−15.9
C veins	2-2	Quartz	13.6	−117.6	200	1.9	−12.1
C veins	2-2	Quartz	13.7	−124.4	240	4.3	−15.9
C veins	2-2	Quartz	13.5	−124.6	200	1.8	−12.0

Table 3: Sulfur isotope data for ore minerals of the Bairendaba Ag-Zn-Pb deposit.

Sample	Mineral	$\delta^{34}S_{CDT}$/‰	Sample location
BR1-1	Pyrite	0.2	Number 1 orebody at 1275 m level
BR1-2	Pyrite	−0.1	Number1 orebody at 1145 m level
BR2-1	Pyrrhotite	1.5	Number 1 orebody at 1275 m level
BR2-2	Pyrrhotite	1.4	Number 1 orebody at 1145 m level
BR3	Sphalerite	0.5	Number 1 orebody at 1270 m level
BR4	Sphalerite	0.9	Number 1 orebody at 1142 m level
BR5	Galena	0.5	Number 1 orebody at 1270 m level
BR6	Galena	0.5	Number 1 orebody at 1142 m level

Therefore, we propose a magmatic source for sulfur, with minor crustal contamination.

Lead (Pb) isotopes provide additional information to constrain the source(s) of ore-forming materials in deposits [65, 66]. A compilation of data for sulfide minerals from the Bairendaba Ag-Zn-Pb deposit shows values of 18.3–18.5 ($^{206}Pb/^{204}Pb$), 15.5–15.7 ($^{207}Pb/^{204}Pb$), and 38.1–38.6 ($^{208}Pb/^{204}Pb$) [17, 33] that are richer in uranogenic Pb but poorer in thorogenic Pb. The majority of Pb isotope data for the ore sulfides cluster between the orogenic and mantle growth curves on an uranogenic plot, with a small population above the orogenic growth curve (Figure 9(a)). A thorogenic plot shows Pb isotope data for the ore sulfides are close to the orogenic growth line (Figure 9(b)). We interpret these data to reflect a hybrid crustal-mantle source of lead.

Additional Pb isotope data exist for unmineralized rock units in the region [17, 49–51] and allow for a comparison with the Bairendaba deposit. These data plot over a broader range than the ore sulfides from the Bairendaba deposit (Figures 9(a) and 9(b)). Generally, if Pb from different geological units is derived from the same source, the Pb isotope compositions and variation trends should be similar. The Pb isotope composition of the Bairendaba ores is clearly different from that of gneiss and partially overlaps with the Beidashan granite and Permian strata. The Pb isotope composition of the Bairendaba ores shows a linear correlation with, and similar minimum values to, the Beidashan granite, which indicates they may have a common origin. The range in Pb isotope data may result from later contamination.

Given the similar ages of the 139–140 Ma Beidashan granite [30] and the 133 ± 2 Ma mineralization at the Bairendaba deposit [14], we propose the Beidashan granite was a source of heat and ore-forming materials for the deposit. Sulfur isotope data support this view, but Pb isotopes suggest a hybrid crustal-mantle source. Previous studies documented that more than 60% of polymetallic deposits occur in Permian strata of the SGXR [67]. Geochemical analyses of unaltered Permian strata [43, 68] indicate high concentrations of ore-forming materials including Ag, As, Sn, Pb, and Zn (Table 4). Therefore, ore-forming materials in the Bairendaba deposit were derived from both the Beidashan granite and Permian strata.

5.2. Fluid Sources and Evolution of the Hydrothermal System. Fluid inclusion microthermometric data and the different types of inclusions in Stages 1-2 quartz and Stage 3 fluorite at the Bairendaba Ag-Zn-Pb deposit highlight distinct changes in the hydrothermal system with time. Histograms show a sharp decrease in temperature and salinity from Stages 1 to 3 (Figure 6). Fluid inclusion types also record a progressive change from a saline CH_4-rich system to a mixed $CH_4 + CO_2$ system and late low-salinity water-dominant system.

The presence of CH_4 in fluid inclusions of Stages 1-2 at the Bairendaba deposit requires further discussion. Mineralizing

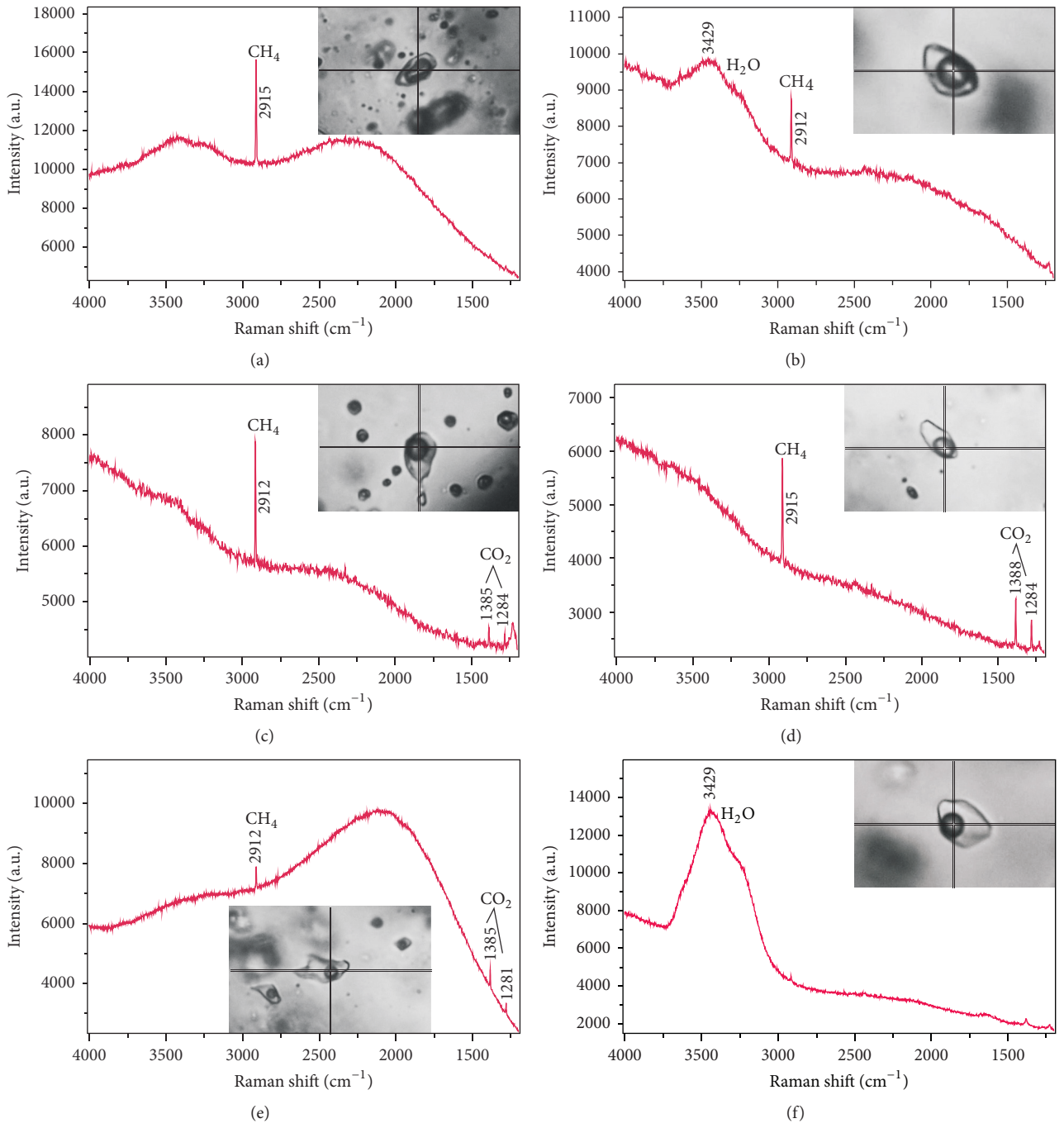

FIGURE 7: Laser Raman microspectrometry of primary fluid inclusions in hydrothermal quartz and fluorite of the Bairendaba Ag-Zn-Pb deposit. ((a), (b)) Type I inclusions in Stage 1 quartz. ((c), (d)) Type II inclusions in Stage 2-1 quartz. (e) Type II inclusions in Stage 2-2 quartz. (f) Type III inclusions in Stage 3 fluorite.

fluids for other deposits in the SGXR, including the Weilasituo deposit that occurs 4 km to the west of Bairendaba, also contain CH_4 [69]. Previous studies have proposed that CH_4 originated from a deep source of reduced magma. Fluids exsolved from a reduced melt would be enriched in CH_4 and not CO_2 [70–75]. However, cross-cutting relationships indicate dolerite dykes, derived from a deep source, predate the mineralization [14]. The metamorphism of organic-rich formations could also be a source of CH_4 [41, 76]. As the Permian strata are carbon-rich [21], metamorphism caused by late magmatic activity could have produced CH_4 in mineralizing fluids.

Carbon isotope data for quartz and calcite provide additional clues to the source of CH_4 in ore-forming fluids. Hydrothermal quartz analyzed in this study has a broader range of $\delta^{13}C_{PDB}$ values (−15.9‰ to −12‰) than calcite

Table 4: Element abundance in lithologies of Permian strata, SGXR [43].

Element content	Sandstone (ppm)	Slate (ppm)	Arkose (ppm)	Tuff (ppm)	Clarke (ppm)
Mn	933.16	972.24	825.08	957.55	950.00
V	96.85	96.07	69.42	121.00	135.00
Ti	4241.18	4457.84	3457.62	4464.76	5700.00
Cu	43.41	52.12	40.50	44.60	55.00
Pb	15.35	14.87	69.88	11.80	12.60
Zn	81.27	84.17	76.73	81.46	70.00
As	9.61	11.61	9.46	10.94	1.80
Sn	5.18	6.38	5.48	3.23	2.00
Ag	0.18	0.17	0.15	0.17	0.07
Mo	1.42	1.19	1.25	1.19	1.50
Ni	23.60	24.27	14.61	15.35	75.00

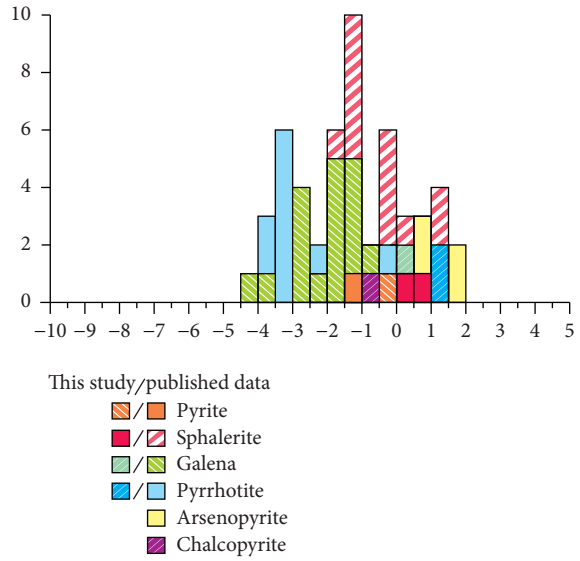

Figure 8: Histogram of S isotope data, Bairendaba Ag-Zn-Pb deposit. The published S isotope data are from Ouyang [33], Jiang et al. [17], and Mei et al. [47].

(−13.5‰ to −12.8‰) [33]. Although quartz and calcite represent different stages of mineralization at the Bairendaba Ag-Zn-Pb deposit, most samples plot within the field of organically derived carbon on a $\delta^{13}C_{PDB}$ versus $\delta^{18}O_{SMOW}$ diagram (Figure 10). Therefore, we propose that metamorphism of carbon-rich Permian strata was the source of CH_4 in the ore-forming fluids.

A potentially important point to consider is why fluids in Stage 1 are CH_4-rich, whereas CO_2 increases and CH_4 decreases in Stage 2. Rios et al. [77] documented that fluid inclusions in ore-bearing quartz veins at a shallow level in the Pedra Preta wolframite deposit, southern Pará, are rich in CH_4 compared with deep samples containing high levels of CO_2, but minor CH_4. This distribution of different fluid-inclusion types was attributed to the deep Musa intrusion and the oxidation of CH_4 to CO_2 following the reaction: $CH_{4(g)} + 2O_{2(g)} = CO_{2(g)} + H_2O_{(g)}$. This reaction confirms how an increase in fO_2 of a hydrothermal system could change a reduced CH_4-rich fluid into an oxidized fluid containing CO_2. However, a change in fO_2 could also result from the addition of oxidized meteoric water to the hydrothermal system during mineralization.

The possibility of having fluids, with different origins, in the hydrothermal system that formed the Bairendaba deposit is addressed using H and O isotope data. Ranges in values of δD and calculated $\delta^{18}O_{H2O}$ (Table 2) for hydrothermal quartz, calcite, and fluorite suggest multiple sources of oxygen. Values of δD for Stage 1 quartz are lighter than those for magmatic water (−50‰ to −80‰) [64] and when paired with calculated $\delta^{18}O_{H2O}$ values, they plot under the magmatic water box on a δD versus $\delta^{18}O_{H2O}$ diagram (Figure 11). Data for Stage 2-1 and Stage 2-2 quartz show a slight shift towards the meteoric water line. In contrast, O-H isotope data for paragenetically younger calcite and fluorite define a trend towards the meteoric water line (Figure 11). The differences in these data could reflect magma degassing, fluid mixing, and/or water-rock interaction.

Magma degassing can produce significant ranges in δD and δ^{34}S through fractionation [78]. Different degrees of degassing, in an open system, could cause δD for ore-forming fluids derived from magmatic water to be depleted by 50%–80% [79]. Fractionation of sulfur through magma degassing will also lead to a significant decrease in δ^{34}S for different sulfide minerals [80]. However, δ^{34}S data for the Bairendaba deposit have a limited range and this indicates fractionation did not occur and produce the observed δD depletion.

The mixing of meteoric water with magmatically derived ore fluids will cause a decrease in δD, as indicated by isotope data for Stages 1–3 at the Bairendaba deposit. Values of δD ranging from −75‰ to −132‰ [33] are intermediate between the δD of magmatic water (−50‰ to −80‰) [64] and local Mesozoic meteoric water in the SGXR (−149‰) [25]. Therefore, fluid mixing could account for the δD depletion.

Another possibility involves fluid interaction with common rock-forming minerals such as biotite and hornblende, which can have δD of −170‰ [81]. Water-rock interaction will lead to isotopic exchange and result in a decrease of δD for the evolved fluid [57, 82].

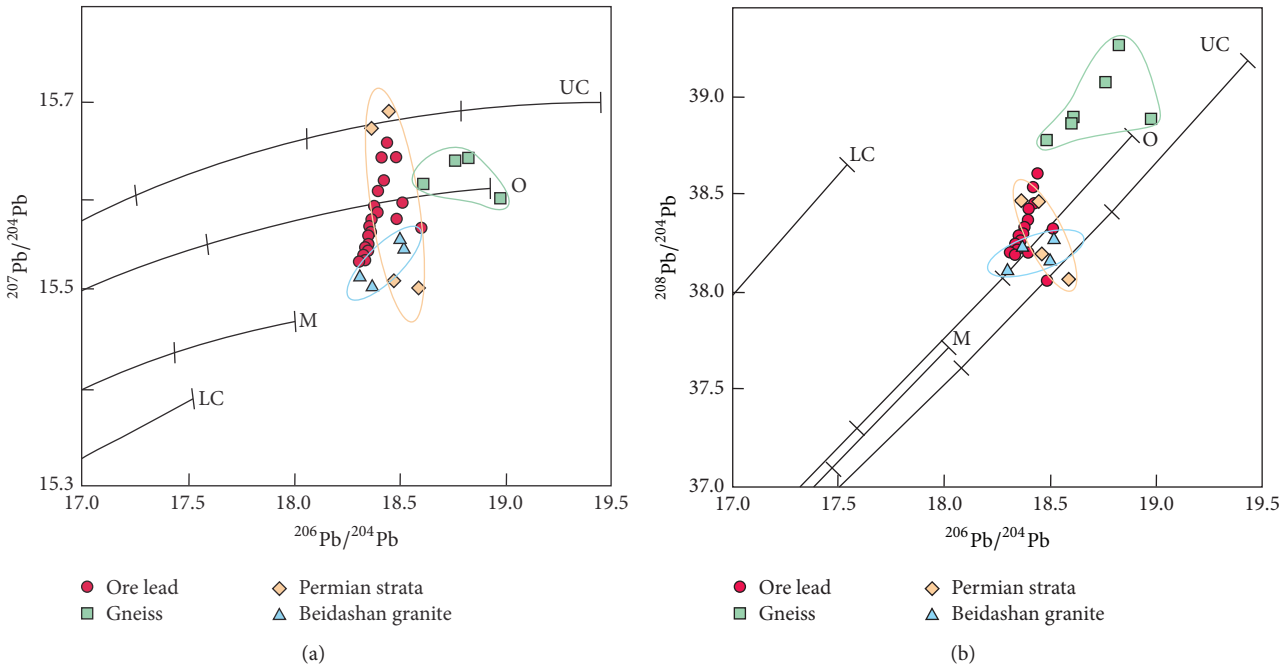

FIGURE 9: Lead isotope compositions for sulfides and host rocks in the Bairendaba Ag-Zn-Pb deposit. (a) $^{207}Pb/^{204}Pb$ versus $^{206}Pb/^{204}Pb$ plot; (b) $^{208}Pb/^{204}Pb$ versus $^{206}Pb/^{204}Pb$ plot. UC (upper crust), O (orogen), M (mantle), and LC (lower crust). The average growth curve is from Zartman and Doe [48]. Lead isotope data for ore are from Ouyang [33] and from Jiang et al. [17], Chu et al. [49], and Zeng et al. [50] for Permian strata; Jiang et al. [17] for gneiss; and Jiang et al. [17] and Wang [51] for the Beidashan granite.

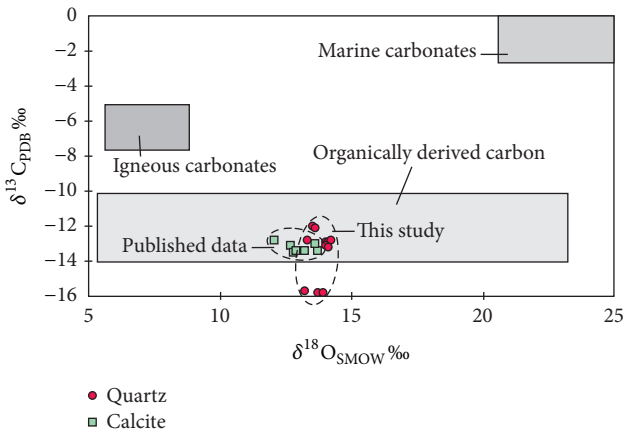

FIGURE 10: $\delta^{13}C$ versus $\delta^{18}O$ diagram showing the distribution of carbon and oxygen isotope data for the Bairendaba Ag-Zn-Pb deposit relative to fields for marine and magmatic carbonates [52] and organically derived carbon [53]. The data for calcite are from Ouyang [33].

At the Bairendaba deposit, water-rock interaction is suggested by the limited range of $\delta^{18}O_{H2O}$ values and CH_4-rich fluid in Stage 1. An evolved meteoric water entering the hydrothermal system during Stages 2-3 could explain $\delta^{18}O$ values that trend towards the meteoric water line. Fluid inclusion data recording a decrease in CH_4 content, Th, and salinity from Stages 1-3 support the addition of meteoric water to the hydrothermal system with time. Therefore, we conclude the ore fluid was derived from a magmatic source that interacted with crustal rocks and mixed with meteoric water, which became more pronounced in the hydrothermal system during Stage 3.

5.3. Genesis of the Bairendaba Ag-Zn-Pb Deposit. Fluid inclusion and stable isotope data need to be interpreted in context with geologic relationships, at both a regional and deposit scale, to develop a coherent genetic model. The Bairendaba Ag-Zn-Pb deposit occurs within a region that underwent compressional tectonism caused by the pre-Mesozoic collision of the Siberian and North China plates [29, 83]. A structural fabric of NE and EW trending faults formed during this deformational event. By the early Mesozoic period, the closing of Paleo-Asian oceans and final collision between the Siberian Plate and north China resulted in a gradual transition to the Circum-Pacific tectonic domain [84–87].

During the Early Cretaceous period, subduction of the Pacific Plate beneath the Eurasian Plate caused large-scale volcanic events across NE China and at the Bairendaba deposit. Zircon U-Pb ages for these intrusions are 119 to ~ 140 Ma, with a peak at 125–140 Ma [29, 88, 89]. Geochemical characteristics of the intrusive rocks, which are closely related to mineralization in the region, show a uniform isotopic composition of low $^{87}Sr/^{86}Sr(i)$ and high $\varepsilon Nd(t)$ values [90–92]. This is a result of melting and differentiation of mantle materials and contamination by crustal rocks [90, 93]. The identification of metamorphic core complexes [94], bimodal volcanic rocks [94–97], and widespread anorogenic A-type granites [93] suggest Early Cretaceous magmatism

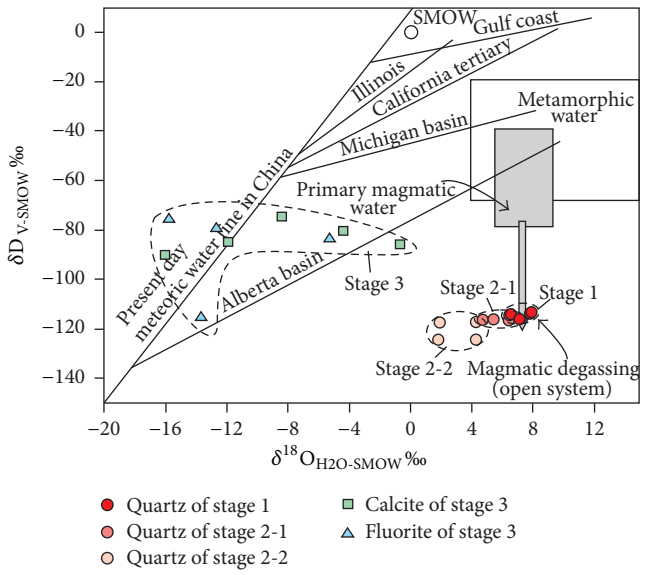

FIGURE 11: δD versus δ^{18}O diagram for quartz, calcite, and fluorite representing different stages of mineralization at the Bairendaba Ag-Zn-Pb deposit. The data of calcite and fluorite are from Ouyang [33]. Trend lines included for reference are based on data from the Gulf Coast, Illinois, and Michigan basins [54]; Alberta Basin [55]; and California Tertiary geothermal brines [56]. Fields for metamorphic and primary magmatic waters are from Taylor Jr. [57]. Data used to derive a present-day meteoric water line for China are from Chen and Wang [58].

and related mineralization occurred while the SGXR was undergoing extension [98–102].

The timing of mineralization at different ore deposits in the SGXR is documented by Ar-Ar dating of sericite and muscovite, K-Ar dating of sericite, Re-Os dating of molybdenite, and U-Pb dating of hydrothermal zircon [14, 103–105]. These data indicate the interval of 120 to ~135 Ma is an important metallogenic period for the SGXR. Deposits of this age have similar δ^{18}O and δD data that support ore-forming fluids of magmatic origin mixing with meteoric water. Sulfur isotope data for these deposits also indicate a magmatic-hydrothermal origin [1, 4, 106–108]. Although different types of mineralization and alteration are evident in the region, all likely represent a metallogenic event that occurred during an extensional tectonic regime.

A geodynamic model involving crustal thinning and magmatism is proposed for mineralization in the region, including the Bairendaba Ag-Zn-Pb deposit. Mineralization coincided with large-scale lithospheric thinning and magmatic underplating during the Early Cretaceous period [29, 109]. Asthenospheric upwelling initiated crustal thinning, reactivated structures, and provided a heat source to circulate fluids on a regional scale. Crust-mantle interaction generated large bodies of silicic magma associated with mineralization. The process of magma emplacement and crystallization evolved fluids rich in volatiles and metals. These fluids caused alteration (e.g., silicification and chloritization), and the convective circulation of groundwater around cooling igneous intrusions leached additional metals from country rocks.

Hydrothermal fluids in a relatively closed, reducing environment transported Ag, Zn, and Pb as aqueous Cl^- and HS^- complexes [81, 110]. Factors causing the deposition of metals from ore-forming fluids in the Bairendaba deposit include a change in temperature, water-rock interaction, and fluid mixing. Fluid inclusions in samples of Stage 1 and Stage 3 mineralization record Th values of 242–395°C and 138–213°C (Table 1), respectively. As the solubility of Cl^- and HS^- complexes is correlated with temperature, the documented decrease in Th for Stages 1–3 would cause hydrothermal fluids to precipitate metals [111].

Water-rock interaction at the Bairendaba deposit is indicated by O-H isotope data (Figure 11). Reactions between the wall rocks and hydrothermal fluids would have included the following: $PbCl_n^{(n-2)-}{}_{(aq)} + HS^-{}_{(aq)} = PbS_{(galena)} + nCl^- + H^+{}_{(aq)}$ and $ZnCl_n^{(n-2)-}{}_{(aq)} + HS^-{}_{(aq)} = ZnS_{(sphalerite)} + nCl^-{}_{(aq)} + H^+{}_{(aq)}$ [112]. Metasomatism would have consumed H^+ and driven the reaction forward. A corresponding increase in pH would have destabilized metal complexes and caused sulfide minerals to precipitate.

The occurrence of fluid mixing at the Bairendaba deposit is supported by the change in fluid inclusion types, Th, and salinities from Stages 1-3 (Figures 5 and 6). The initial magmatic fluid in Stage 1 mixed with progressively greater amounts of evolved meteoric water in Stages 2-3. The mixing of fluids with different sources in the hydrothermal system would have occurred according to the following reactions: $PbCl_n^{(n-2)-}{}_{(aq)} + 2H_2S_{(g)} + 1/2O_{2(g)} = PbS_2 + 2H^+{}_{(aq)} + H_2O_{(l)} + nCl^-{}_{(aq)}$ and $ZnCl_n^{(n-2)-}{}_{(aq)} + 2H_2S_{(g)} + 1/2O_{2(g)} = ZnS_2 + 2H^+{}_{(aq)} + H_2O_{(l)} + nCl^-{}_{(aq)}$ [113]. A decrease in H^+ and Cl^- concentrations of the hydrothermal fluid due to mixing would drive the reactions forward and increase fO_2 of a hydrothermal system, leading to the precipitation of sulfide minerals. These processes of ore deposition were common in the SGXR, where sulfide minerals precipitated within extensional structures produced by regional tectonic processes, forming large deposits.

6. Conclusions

Distinct populations of fluid inclusions in Stage 1–3 quartz and fluorite at the Bairendaba deposit record a progressive change from a saline CH_4-rich system to a mixed $CH_4 + CO_2$ system and a late-stage system dominated by low-salinity water. The decrease in fluid salinity was accompanied by a decrease in temperature.

Ore-forming fluids with a magmatic source interacted with wall rocks and mixed with meteoric water, as evidenced by changes in values for $\delta^{18}O_{fluid}$ and δD_{fluid}. Sulfur isotope data indicate a magmatic source, whereas $\delta^{13}C$ values for fluid inclusions in hydrothermal quartz support the derivation of carbon from organic-rich Permian strata.

The Bairendaba Ag-Zn-Pb deposit is a typical mesothermal deposit that formed in an extensional environment related to Early Cretaceous subduction of the Pacific Plate.

Conflicts of Interest

The authors declare no conflicts of interest regarding the publication of this paper.

Acknowledgments

This work was supported by the Shandong Gold Group Co. Ltd. (Project no. SJ201309). The authors are grateful to the staff of the Shandong Gold Group Co. Ltd. and the Inner Mongolia Yindu Mining Co. Ltd. for assistance with field work and access to the Bairendaba Mine. They are also grateful to Dr. Liu for assistance with stable isotope analyses at the Analytical Laboratory Beijing Research Institute of Uranium Geology.

References

[1] J. B. Wang, Y. W. Wang, L. J. Wang, and T. Uemoto, "Tin-polymetallic mineralization in the southern part of the Da Hinggan Mountains, China," *Resource Geology*, vol. 51, no. 4, pp. 283–291, 2001.

[2] Q. Zeng, J. Liu, C. Yu, J. Ye, and H. Liu, "Metal deposits in the da Hinggan Mountains, NE China: Styles, characteristics, and exploration potential," *International Geology Review*, vol. 53, no. 7, pp. 846–878, 2011.

[3] M. G. Zhai and M. Santosh, "Metallogeny of the North China Craton: link with secular changes in the evolving Earth," *Gondwana Research*, vol. 24, no. 1, pp. 275–297, 2013.

[4] X. Zhu, Q. Zhang, Y. He, C. Zhu, and Y. Huang, "Hydrothermal source rocks of the Meng' entaolegai Ag-Pb-Zn deposit in the granite batholith, inner Mongolia, China: Constrained by isotopic geochemistry," *Geochemical Journal*, vol. 40, no. 3, pp. 265–275, 2006.

[5] W. Zhang, F. Nie, S. Liu et al., "Characteristics and genesis of mineral deposits in East Ujimqin Banner, western segment of the Great Xing'an Mountains, NE China," *Journal of Asian Earth Sciences*, vol. 97, pp. 459–471, 2015.

[6] Y. Q. Chen, D. Zhou, and L. F. Guo, "Genetic study on the huaaobaote Pb-Zn-Ag polymetallic deposit in Inner Mongolia: evidence from fluid inclusions and S, Pb, H, O isotopes," *Journal of Jilin University (Earth Science Edition)*, vol. 44, no. 5, pp. 1478–1491, 2014 (Chinese).

[7] J. J. Xu, Y. Lai, D. Cui et al., "Characteristics and evolution of ore-forming fluids of the Daolundaba copper-poly-metal deposit, Inner Mongolia," *Acta Petrologica Sinica*, vol. 25, no. 11, pp. 2957–2972, 2009.

[8] Y. S. Kuang, G. R. Zheng, and M. J. Lu, "Basic characteristics of Shuangjianzishan sliver polymetallic deposit in Chifeng City, Inner Mongolia," *Mineral Deposits*, vol. 33, no. 4, pp. 847–856, 2014.

[9] G. B. Wu, J. M. Liu, Q. D. Zeng et al., "Occurrences of silver in the Shuangjianzishan Pb-Zn-Ag deposit and its implications for mineral processing," *Earth Science Frontiers*, vol. 21, pp. 105–115, 2014.

[10] J. F. Sheng and X. Z. Fu, *Metallogenetic Environment and Geological Characteristics of Copper-Polymetallic Ore Deposits in Middle Part of Da Hinggan Mts*, Seismological Publishing House, Beijing, China, 1999.

[11] Q. Zhang, X. Z. Zhan, Y. Z. Qiu et al., "Lead isotopic compostion and lead source of Meng'entaolegai Ag-Pb-Zn-In deposit in Inner Mongolia," *Geochimica*, vol. 31, no. 3, pp. 253–258, 2002 (Chinese).

[12] A. Q. Sun, S. Y. Niu, B. J. Ma et al., "A comparative study of ore-forming structures in Bairendaba and Weilatiuo silver-polymetallic deposits of Inner Mongolia," *Journal of Jilin University (Earth Science Edition)*, vol. 41, no. 6, pp. 1785–1805, 2011 (Chinese).

[13] J. Wang, Q. Y. Hou, Y. L. Chen et al., "Fluid inclusion study of the Weilasituo Cu polymetal deposit in Inner Mongolia," *Geoscience*, vol. 24, no. 5, pp. 847–855, 2010 (Chinese).

[14] X. F. Pan, L. J. Guo, S. Wang et al., "Laser microprobe Ar - Ar dating of biotite from the Weilasituo Cu-Zn polymetallic deposit in Inner Mongolia," *Acta Petrologica ET Mineralogica*, vol. 28, no. 5, pp. 473–479, 2009 (Chinese).

[15] Y. Chang and Y. Lai, "Study on characteristics of ore-forming fluid and chronology in the Yindu Ag-Pb-Zn polymetallic ore deposit, Inner Mongolia," *Acta Scientiarum Naturalium Universitatis Pekinensis*, vol. 46, no. 4, pp. 581–593, 2010 (Chinese).

[16] Y. F. Liu, S. H. Jiang, and Y. Zhang, "The SHRIMP zircon U-Pb dating and geological features of Bairendaba diorite in the Xilinhaote area, Inner Mongolia, China," *Geological Bulletin of China*, vol. 29, no. 5, pp. 688–696, 2010 (Chinese).

[17] S. H. Jiang, F. J. Nie, Y. F. Liu et al., "Sulfur and lead isotopic compositions of Bairendaba and Weilasituo silver-polymetallic deposits, Inner Mongolia," *Mineral Deposits*, vol. 29, no. 1, pp. 101–112, 2010 (Chinese).

[18] J. M. Liu, R. Zhang, Q. Z. Zhang et al., "The regional metallogeny of Dahingganling, China," *Earth Science Frontiers*, vol. 11, pp. 269–277, 2004 (Chinese).

[19] F. Y. Sun and L. Wang, "Ore -forming conditions of bairendaba Ag-Pb-Zn polymetallic ore deposit, Inner Mongolia," *Journal of Jilin University (Earth Science Edition)*, vol. 38, no. 3, pp. 376–383, 2008 (Chinese).

[20] L. J. Guo, Y. L. Xie, Z. Q. Hou et al., "Geology and ore fluid characteristics of the Bairendaba silver polymetallic deposit in Inner Mongolia," *Acta Petrologica et Mineralogica*, vol. 28, no. 1, pp. 26–36, 2009 (Chinese).

[21] G. Shi, D. Liu, F. Zhang et al., "SHRIMP U-Pb zircon geochronology and its implications on the Xilin Gol Complex, Inner Mongolia, China," *Chinese Science Bulletin*, vol. 48, no. 24, pp. 2742–2748, 2003.

[22] Y. F. Liu, *Metallogenic study of bairendaba Ag polymetallic deposit in hexigten banner, Inner Mongolia [M. S. thesis]*, Chinese Academy of Geological Sciences, Beijing, China, 2009.

[23] B. H. Huang, *Carboniferous and Permian Systems and Floras in the Da Hinggan Range*, Geology Publishing House, Beijing, China, 1993.

[24] G. Qin, Y. Kawachi, L. Zhao, Y. Wang, and Q. Ou, "The upper Permian sedimentary facies and its role in the Dajing Cu-Sn deposit, Linxi County, Inner Mongolia, China," *Resource Geology*, vol. 51, no. 4, pp. 293–305, 2001.

[25] D. Q. Zhang, "Geological setting and ore types of the Huanggang-ganzhuermiao Tin, sliver and polymetallic ore zone in eastern Inner Mongolia," *Bulletin of the Institude of Mineral Deposits Chinese Academy of Geological Sciences*, vol. 22, no. 1, pp. 42–54, 1989 (Chinese).

[26] S. Y. Fan, H. R. Mao, X. D. Zhang et al., "Stratigraphic geochemistry of permian strata in the central da hinggan mountains and its metallogenic significance," *Regional Geology of China*, vol. 16, no. 1, pp. 89–97, 1997 (Chinese).

[27] F. Y. Sheng, X. Z. Fu, and H. N. Li, *Metallogenic environment and geological characteristics of copper polymetallic deposit in the middle section of Daxing'an Mountains*, Seismological Press, Beijing, China, 1999.

[28] Bureau of Geology and Mineral Resources of Inner Mongolia (BGMRIM), *Regional geology of Nei Mongol (Inner Mongolia) Autonomous Region. Geologymemoir Seria 2, 25*, Geology Publish House, Beijing, China, 1991.

[29] F.-Y. Wu, D.-Y. Sun, W.-C. Ge et al., "Geochronology of the Phanerozoic granitoids in northeastern China," *Journal of Asian Earth Sciences*, vol. 41, no. 1, pp. 1–30, 2011.

[30] Y. F. Liu, F. J. Nie, S. H. Jiang et al., "Bairendaba Pb-Zn-Ag Polymetallic deposit in Inner Mongolia: the mineralization zoning and its origin," *Journal of Jilin University (Earth Science Edition)*, vol. 42, no. 4, pp. 1055–1068, 2012 (Chinese).

[31] X. Zhang, S. A. Wilde, H. Zhang, and M. Zhai, "Early Permian high-K calc-alkaline volcanic rocks from NW Inner Mongolia, North China: Geochemistry, origin and tectonic implications," *Journal of the Geological Society*, vol. 168, no. 2, pp. 525–543, 2011.

[32] Y. Liu, S. H. Jiang, Z. G. Zhang et al., "Mineragrahy of bairendaba and weilasituo silver-polymetallic deposits in Inner Mongolia," *Mineral Deposits*, vol. 30, no. 5, pp. 837–854, 2011 (Chinese).

[33] H. G. Ouyang, *Metallogenesis of bairendaba-weilasituo silver polytmetallic deposit and its geodynamic setting, in the southern segment of Great Xing'an Range, NE China [Doctoral, thesis]*, China University of Geosciences, Beijing, China, 2013.

[34] H. F. Xu, "Study on bairendaba polymetallic minerals of keshiketeng county," *Journal of Inner Mongolia Radio and TV University*, vol. 25, no. 2, p. 41, 2004 (Chinese).

[35] L. M. Xiao, *Discussion on characteristics and genesis of formation of bairendaba polymetal Ag deposit, chifeng, Inner Mongolia [M.S. thesis]*, Jilin University, Changchun, China.

[36] R. J. Bodnar, "Revised equation and table for determining the freezing point depression of H2O-Nacl solutions," *Geochimica et Cosmochimica Acta*, vol. 57, no. 3, pp. 683-684, 1993.

[37] R. N. Clayton and T. K. Mayeda, "The use of bromine pentafluoride in the extraction of oxygen from oxides and silicates for isotopic analysis," *Geochimica et Cosmochimica Acta*, vol. 27, no. 1, pp. 43–52, 1963.

[38] I. Friedman, "Deuterium content of natural waters and other substances," *Geochimica et Cosmochimica Acta*, vol. 4, no. 1-2, pp. 89–103, 1953.

[39] B. W. Robinson and M. Kusakabe, "Quantitative preparation of sulfur dioxide, for34S/32S analyses, from sulfides by combustion with cuprous oxide," *Analytical Chemistry*, vol. 47, no. 7, pp. 1179–1181, 1975.

[40] E. Roedder, "Fluid inclusions," *Review of Mineral*, vol. 12, p. 644, 1984.

[41] L. S. Hollister and R. C. Burruss, "Phase equilibria in fluid inclusions from the Khtada Lake metamorphic complex," *Geochimica et Cosmochimica Acta*, vol. 40, no. 2, pp. 163–175, 1976.

[42] C. Ramboz, M. Pichavant, and A. Weisbrod, "Fluid immiscibility in natural processes: Use and misuse of fluid inclusion data. II. Interpretation of fluid inclusion data in terms of immiscibility," *Chemical Geology*, vol. 37, no. 1-2, pp. 29–48, 1982.

[43] Y. H. Yang, S. E. Lian, and T. Ba, "Stratigrahic geochemistry of permian strata in the central da hinggan mountains and its metallogenic significance," *Western Resources*, vol. 2, pp. 178–181, 2012 (Chinese).

[44] P. L. F. Collins, "Gas hydrates in CO2-bearing fluid inclusions and the use of freezing data for estimation of salinity," *Economic Geology*, vol. 74, no. 6, pp. 1435–1444, 1979.

[45] A. M. Dreher, R. P. Xavier, B. E. Taylor, and S. L. Martini, "New geologic, fluid inclusion and stable isotope studies on the controversial Igarapé Bahia Cu-Au deposit, Carajás Province, Brazil," *Mineralium Deposita*, vol. 43, no. 2, pp. 161–184, 2008.

[46] A. V. Volkov, N. E. Savva, A. A. Sidorov et al., "Shkol'noe gold deposit, the Russian Northeast," *Geology of Ore Deposits*, vol. 53, no. 1, pp. 1–26, 2011.

[47] W. Mei, X. B. Lv, R. K. Tang et al., "Ore-forming fluid and its evolution of Bairendaba-Weilasituo deposits in west slope of southern Great Xing'an Range," *Earth Science (Journal of China University of Geosciences)*, vol. 40, no. 1, pp. 145–162, 2015.

[48] R. E. Zartman and B. R. Doe, "Plumbotectonics-the model," *Tectonophysics*, vol. 75, no. 1-2, pp. 135–162, 1981.

[49] X. Chu, W. Huo, and X. Zhang, "Sulfur, carbon and lead isotope studies of the Dajing polymetallic deposit in Linxi County, Inner Mongolia, China - Implication for metallogenic elements from hypomagmatic source," *Resource Geology*, vol. 51, no. 4, pp. 333–344, 2001.

[50] Q. Zeng, J. Liu, J. Liu et al., "Geology and lead-isotope study of the baiyinnuoer Zn-Pb-Ag deposit, south segment of the Da Hinggan mountains, Northeastern China," *Resource Geology*, vol. 59, no. 2, pp. 170–180, 2009.

[51] J. Wang, *Chronology and geochemistry of granitoid for the weilasituo copperpolymetal deposit in Inner Mongolia [M.S. thesis]*, China University of Geosciences, Beijing, China, 2009.

[52] J. W. Valley, "Stable isotope geochemistry of metamorphic rocks," in *Stable Isotopes in High Temperature Geological Processes*, J. W. Valley, H. P. Taylor, J. R. O'Neil et al., Eds., vol. 16, pp. 445–489, Reviews in Mineralogy, 1986.

[53] F. J. Longstaffe, "Stable isotopes as tracers in clastic diagenesis. Short course in burial diagenesis," in *Mineral Association of Canada Short Course*, I. E. Hutcheon, Ed., pp. 201–284, 1989.

[54] R. N. Clayton, I. Friedman, D. L. Graf et al., "The origin of saline formation waters: 1. Isotopic composition," *Journal of Geophysical Research*, vol. 71, no. 16, pp. 3869–3882, 1966.

[55] B. Hitchon and I. Friedman, "Geochemistry and origin of formation waters in the western Canada sedimentary basin-I. Stable isotopes of hydrogen and oxygen," *Geochimica et Cosmochimica Acta*, vol. 33, no. 11, pp. 1321–1349, 1969.

[56] Y. K. Kharaka, F. A. F. Berry, and I. Friedman, "Isotopic composition of oil-field brines from Kettleman North Dome, California, and their geologic implications," *Geochimica et Cosmochimica Acta*, vol. 37, no. 8, pp. 1899–1908, 1973.

[57] H. P. Taylor Jr., "The application of oxygen and hydrogen isotope studies to problems of hydrothermal alteration and ore deposition," *Economic Geology*, vol. 69, no. 6, pp. 843–883, 1974.

[58] J. Chen and H. N. Wang, *Geochemistry*, Science Press, Beijing, China, 2004.

[59] R. N. Clayton, J. R. O'Neil, and T. K. Mayeda, "Oxygen isotope exchange between quartz and water," *Journal of Geophysical Research*, vol. 77, no. 17, pp. 3057–3067, 1972.

[60] X. D. Wang, X. B. Lv, W. Mei et al., "Characteristics and evolution of ore-forming fluids in Bairendaba Ag-Pb-Zn polymetallic deposit, Inner Mongolia," *Mineral Deposits*, vol. 33, no. 2, pp. 406–418, 2014 (Chinese).

[61] B. R. Doe and J. S. Stacey, "The application of lead isotopes to the problems of ore genesis and ore prospect evaluation: A review," *Economic Geology*, vol. 69, no. 6, pp. 757–776, 1974.

[62] R. O. Rye and H. Ohmoto, "Sulfur and carbon isotopes and ore genesis: A review," *Economic Geology*, vol. 69, no. 6, pp. 826–842, 1974.

[63] J. Hoefs, *Stable Isotope Geochemistry*, Springer, Berlin, Germany, 6th edition, 2009.

[64] H. Ohmoto and R. O. Rye, *Isotopes of sulfur and carbon*, John Wiley and Sons, New York, NY, USA, 1979.

[65] F. P. Bierlein and N. J. McNaughton, "Pb isotope fingerprinting of mesothermal gold deposits from central Victoria, Australia: Implications for ore genesis," *Mineralium Deposita*, vol. 33, no. 6, pp. 633–638, 1998.

[66] Y. Qiu and N. J. McNaughton, "Source of Pb in orogenic lode-gold mineralisation: Pb isotope constraints from deep crustal rocks from the southwestern Archaean Yilgarn Craton, Australia," *Mineralium Deposita*, vol. 34, no. 4, pp. 366–381, 1999.

[67] G. F. Yang, "Geological formation and ore-controlling process of permain system in the southern part of Dahingganling, Inner Mongolia," *Mineral Resources and Geology*, vol. 2, no. 10, pp. 120–125, 1996 (Chinese).

[68] S. Y. Fan, H. Y. Mao, X. D. Zhang et al., "Stratigrahic geochemistry of Permian strata in the central Da Hinggan Mountains and its metallogenic significance," *Regional Geology of China*, vol. 1, no. 16, pp. 89–97, 1997 (Chinese).

[69] H. Ouyang, J. Mao, M. Santosh, Y. Wu, L. Hou, and X. Wang, "The Early Cretaceous Weilasituo Zn-Cu-Ag vein deposit in the southern Great Xing'an Range, northeast China: Fluid inclusions, H, O, S, Pb isotope geochemistry and genetic implications," *Ore Geology Reviews*, vol. 56, pp. 503–515, 2014.

[70] D. L. Hall and R. J. Bodnar, "Methane in fluid inclusions from granulites: A product of hydrogen diffusion?" *Geochimica et Cosmochimica Acta*, vol. 54, no. 3, pp. 641–651, 1990.

[71] S. K. Saxena and Y. Fei, "Fluid mixtures in the CHO system at high pressure and temperature," *Geochimica et Cosmochimica Acta*, vol. 52, no. 2, pp. 505–512, 1988.

[72] L. Q. Xia and R. L. Cao, "Research of the fluid properties from upper mantle in Xilong, Zhejiang," *Chinese Science Bulletin*, vol. 35, no. 11, pp. 844–847, 1990 (Chinese).

[73] L. Su, S. Song, and Z. Wang, "CH4-rich fluid inclusions in the Yushigou mantle peridotite and their implications, North Qilian Mountains, China," *Chinese Science Bulletin*, vol. 44, no. 21, pp. 1992–1995, 1999.

[74] X. F. Pan and W. Liu, "Characeristics and significance of CH4-rich fluid inclusions from the mafic-ultramafic complex at the Xiangshan, eastern Tianshan Mountains, Xinjiang of China," *Acta Petrologica Sinica*, vol. 21, no. 1, pp. 211–218, 2005.

[75] S. Ishihara, "The granitoid series and mineralization," *Economic Geology*, vol. 75, pp. 458–484, 1981.

[76] J. Mullis, "Fluid inclusion studies during very low-grade metamorphism," in *Low Temperature Metamorphism*, M. Frey, Ed., pp. 162–199, Blackie, Glasgow, Scotland, 1987.

[77] F. J. Rios, R. N. Villas, and K. Fuzikawa, "Fluid evolution in the Pedra Preta wolframite ore deposit, Paleoproterozoic Musa granite, eastern Amazon craton, Brazil," *Journal of South American Earth Sciences*, vol. 15, no. 7, pp. 787–802, 2003.

[78] K. I. Shmulovich, D. Landwehr, K. Simon, and W. Heinrich, "Stable isotope fractionation between liquid and vapour in water-salt systems up to 600∘C," *Chemical Geology*, vol. 157, no. 3-4, pp. 343–354, 1999.

[79] B. E. Taylor, "Magmatic volatiles: isotopic variation of C, H, and S," *Reviews in Mineralogy and Geochemistry*, vol. 16, no. 1, pp. 185–225, 1986.

[80] Y.-F. Zheng, "Carbon-oxygen isotopic covariation in hydrothermal calcite during degassing of CO2 - A quantitative evaluation and application to the Kushikino gold mining area in Japan," *Mineralium Deposita*, vol. 25, no. 4, pp. 246–250, 1990.

[81] H. L. Barnes, "Solubilities of ore minerals," in *Geochemistry of hydrothermal ore deposits*, H. L. Barnes, Ed., pp. 404–460, Wiley, 1979.

[82] S. M. F. Sheppard, "Characterization and isotopic variations in natural waters," *Reviews in Mineralogy and Geochemistry*, vol. 16, pp. 165–183, 1986.

[83] B. Xu, J. Charvet, Y. Chen, P. Zhao, and G. Shi, "Middle Paleozoic convergent orogenic belts in western Inner Mongolia (China): Framework, kinematics, geochronology and implications for tectonic evolution of the Central Asian Orogenic Belt," *Gondwana Research*, vol. 23, no. 4, pp. 1342–1364, 2013.

[84] A. M. C. Şengör, B. A. Natal'In, and V. S. Burtman, "Evolution of the Altaid tectonic collage and Palaeozoic crustal growth in Eurasia," *Nature*, vol. 364, no. 6435, pp. 299–307, 1993.

[85] J.-H. Zhang, W.-C. Ge, F.-Y. Wu, S. A. Wilde, J.-H. Yang, and X.-M. Liu, "Large-scale Early Cretaceous volcanic events in the northern Great Xing'an Range, Northeastern China," *Lithos*, vol. 102, no. 1-2, pp. 138–157, 2008.

[86] J. H. Zhang, S. Gao, W. C. Ge et al., "Geochronology of the mesozoic volcanic rocks in the great xing'an range, northeastern china: implications for subduction-induced delamination," *Chemical Geology*, vol. 276, no. 3-4, pp. 144–165, 2010.

[87] W. Xiao, S. Li, M. Santosh, and B.-M. Jahn, "Orogenic belts in Central Asia: Correlations and connections," *Journal of Asian Earth Sciences*, vol. 49, pp. 1–6, 2012.

[88] W. C. Ge, F. Y. Wu, C. Y. Zhou et al., "Zircon U-Pb ages and its significance of mesozoic granites in the wulanhaote region, central da hinggan mountain," *Acta Petrologica Sinica*, vol. 21, no. 3, pp. 749–762, 2005 (Chinese).

[89] W. Liu, X. F. Pan, L. W. Xie et al., "Sources of material for Linxi granitoids, the southern segment of the Da Hinggan Mts.: when and how continental crust grew?" *Acta Perologica Sinica*, vol. 23, no. 2, pp. 441–460, 2007 (Chinese).

[90] W. Liu, W. Siebel, X.-J. Li, and X.-F. Pan, "Petrogenesis of the Linxi granitoids, northern Inner Mongolia of China: Constraints on basaltic underplating," *Chemical Geology*, vol. 219, no. 1-4, pp. 5–35, 2005.

[91] C. D. Xiao, Z. L. Zhang, and L. Q. Zhao, "Nd, Sr and Pb isotope geochemistry of yanshannian granitoids in eastern Inner Mongolia and their origins," *Geology in China*, vol. 31, no. 1, pp. 57–63, 2004 (Chinese).

[92] F. Guo, W. Fan, X. Gao et al., "Sr-Nd-Pb isotope mapping of Mesozoic igneous rocks in NE China: Constraints on tectonic framework and Phanerozoic crustal growth," *Lithos*, vol. 120, no. 3-4, pp. 563–578, 2010.

[93] F.-Y. Wu, D.-Y. Sun, H. Li, B.-M. Jahn, and S. Wilde, "A-type granites in northeastern China: Age and geochemical constraints on their petrogenesis," *Chemical Geology*, vol. 187, no. 1-2, pp. 143–173, 2002.

[94] X. D. Zhang, Q. Yu, and F. J. Chen, "Structural characteristics, origin and evolution of metamorphic core complex in central basement uplift and Xujiaweizi faulted depression in Songliao Basin, northeast China," *Earth Science Frontiers*, vol. 4, pp. 411–419, 2000 (Chinese).

[95] W. C. Ge, Q. Lin, D. Y. Sun et al., "Geochemical characteristics of the mesozoic basalts in da hinggan ling: evidence of the mantle-crust interaction," *Acta Perologica Sinica*, vol. 15, no. 3, pp. 397–407, 1999 (Chinese).

[96] W. H. Zhang, J. Y. Qin, D. H. Zhang et al., "Fluid inclusion indicators in prophyry Au deposits: taking Jinchang gold deposit, Heilongjiang province as an example," *Acta Perologica Sinica*, vol. 24, no. 9, pp. 2011–2016, 2008 (Chinese).

[97] W.-L. Xu, F.-P. Pei, F. Wang et al., "Spatial-temporal relationships of Mesozoic volcanic rocks in NE China: Constraints on tectonic overprinting and transformations between multiple tectonic regimes," *Journal of Asian Earth Sciences*, vol. 74, pp. 167–193, 2013.

[98] Q.-R. Meng, "What drove late Mesozoic extension of the northern China-Mongolia tract?" *Tectonophysics*, vol. 369, no. 3-4, pp. 155–174, 2003.

[99] J. W. Mao, G. Q. Xie, Z. H. Zhang et al., "Mesozoic large-scale metallogenic pulses in north china and corresponding geodynamic settings," *Acta Perologica Sinica*, vol. 21, no. 1, pp. 169–188, 2005 (Chinese).

[100] J. A. Shao, L. Q. Zhang, Q. H. Xiao et al., "Rising of da hinggan mts in mesozoic: a possible mechanism of intracontinental orogeny," *Acta Perologica Sinica*, vol. 21, no. 3, pp. 789–794, 2005 (Chinese).

[101] F. Wang, X.-H. Zhou, L.-C. Zhang et al., "Late Mesozoic volcanism in the Great Xing'an Range (NE China): Timing and implications for the dynamic setting of NE Asia," *Earth and Planetary Science Letters*, vol. 251, no. 1-2, pp. 179–198, 2006.

[102] T. Wang, L. Guo, Y. Zheng et al., "Timing and processes of late Mesozoic mid-lower-crustal extension in continental NE Asia and implications for the tectonic setting of the destruction of the North China Craton: Mainly constrained by zircon U-Pb ages from metamorphic core complexes," *Lithos*, vol. 154, pp. 315–345, 2012.

[103] Z. H. Zhou, L. S. Lv, J. R. Feng et al., "Molybdenite Re-Os ages of Huanggang skam Sn-Fe deposit and their geological significance, Inner Mongolia," *Acta Perologica Sinica*, vol. 26, no. 3, pp. 67–69, 2010 (Chinese).

[104] Q. H. Shu, L. Jiang, Y. Lai et al., "Geochronology and fluid inclusion study of the Aolunhua porphyry Cu-Mo deposit in arhorqin area, Inner Mongolia," *Acta Perologica Sinica*, vol. 25, no. 10, pp. 2601–2614, 2009 (Chinese).

[105] Q. Zeng, J. Liu, S. Chu et al., "Mesozoic molybdenum deposits in the East Xingmeng orogenic belt, northeast China: Characteristics and tectonic setting," *International Geology Review*, vol. 54, no. 16, pp. 1843–1869, 2012.

[106] W. Liu, X. J. Li, and J. Tan, "Fluid mixing in the Dajing Cu-Sn-Ag-Pb-Zn deposits, Inner Mongolia: Evidences from fluid inclusions and stable isotopes," *Science in China (Series D)*, vol. 32, no. 5, pp. 405–414, 2002 (Chinese).

[107] Z. H. Zhou, *Geology and Geochemistry of Huanggang Sn-Fe Deposits, Inner Mongolia*, Chinese Academy of Geological Sciences, Beijing, China, 2011.

[108] H. Ouyang, J. Mao, and M. Santosh, "Anatomy of a large Ag-Pb-Zn deposit in the Great Xing'an Range, northeast China: Metallogeny associated with Early Cretaceous magmatism," *International Geology Review*, vol. 55, no. 4, pp. 411–429, 2013.

[109] J.-H. Zhang, S. Gao, W.-C. Ge et al., "Geochronology of the Mesozoic volcanic rocks in the Great Xing'an Range, northeastern China: Implications for subduction-induced delamination," *Chemical Geology*, vol. 276, no. 3-4, pp. 144–165, 2010.

[110] R. X. Zhu, L. Chen, F. Y. Wu, and J. L. Liu, "Timing, scale and mechanism of the destruction of the North China Craton," *Science China Earth Sciences*, vol. 54, no. 6, pp. 789–797, 2011.

[111] S. A. Wood, D. A. Crerar, and M. P. Borcsik, "Solubility of the assemblage pyrite-pyrrhotite-magnetite-sphalerite-galena-gold-stibnite-bismuthinite-argentite-molybdenite in H2O-NaCl-CO2 Solutions from 200◦ to 350◦C," *Economic Geology*, vol. 82, no. 7, pp. 1864–1887, 1987.

[112] Y. Zhang, R. S. Han, and P. T. Wei, "Mechanisms of Zn-Pb transortation and deposition in the ore-forming fluids of skarn-type Zn-Pb deposit," *Geological Review*, vol. 62, no. 1, pp. 187–201, 2016 (Chinese).

[113] X. Chen, J. J. Liu, Y. C. Li et al., "Mechanisms of lead transortation and deposition in hydrothermal deposits," *Geological Science and Technology Information*, vol. 34, no. 3, pp. 45–57, 2015 (Chinese).